

Reweighted Block Sparsity Regularization for Remote Sensing Images Destriping

Jian-Li Wang , Ting-Zhu Huang , Xi-Le Zhao , Jie Huang , Tian-Hui Ma, and Yu-Bang Zheng

Abstract—Destriping has attracted a lot of interest in the field of remote sensing images processing. Recent research works consider the characteristics of stripes, among which low-rankness and group sparsity regularizations are widely used. However, for real scenarios, these regularizations sometimes fail to work when the underlying assumptions are violated. Motivated by this observation, we propose a novel and flexible regularization, named as the reweighted block sparsity (RBS), for complex stripes (e.g., the partial stripes). RBS divides the stripe layer into several blocks along the stripe-perpendicular direction and boosts the group sparsity of each block, where the sparsity level is adaptively controlled by updating weights. Based on RBS, we further propose a destriping model by integrating RBS and unidirectional total variation regularization, which can better detect and remove complex stripes. Moreover, we develop an alternating direction method of multipliers algorithm to solve the proposed model. Experimental results demonstrate that the proposed method outperforms the state-of-the-art competitors qualitatively and quantitatively.

Index Terms—Alternating direction method of multipliers (ADMM), destriping, remote sensing images, reweighted block sparsity (RBS), unidirectional total variation (UTV).

I. INTRODUCTION

REMOTE sensing images have played an important role in various applications, such as urban planning, agriculture, and military [1]–[5]. However, images observed by many remote sensing imaging systems are inevitably degraded by the stripes [6], [7]. The stripes noise are caused by the nonuniformity in the pixel response through the detector, the difference of air medium, the mechanical movement of sensor, and the change of temperature in the process of image acquisition. [8]. The nonuniformity response includes relative gain and offset variations between neighboring forward and reverse scans of all detectors in the instrument and relative gain, and offset difference among the detectors within a band [9].

Manuscript received March 21, 2019; revised July 13, 2019; accepted August 27, 2019. This work was supported in part by the National Natural Science Foundation of China under Grants 61772003, 61876203, and 11901450, in part by the National Postdoctoral Program for Innovative Talents under Grant BX20180252, and in part by the China Postdoctoral Science Foundation under Grant 2018M643611. (*Corresponding authors:* Ting-Zhu Huang; Xi-Le Zhao.)

J.-L. Wang, T.-Z. Huang, X.-L. Zhao, J. Huang, and Y.-B. Zheng are with the Research Center for Image and Vision Computing, School of Mathematical Sciences, University of Electronic Science and Technology of China, Chengdu 611731, China (e-mail: wangjianli_123@163.com; tingzhuhuang@126.com; xlzhao122003@163.com; happyjie07mo@163.com; zhengyubang@163.com).

T.-H. Ma is with the School of Mathematics and Statistics, Xi'an Jiaotong University, Xi'an, 710049, China (e-mail: nkmtb0307@126.com).

Color versions of one or more of the figures in this article are available online at <http://ieeexplore.ieee.org>.

Digital Object Identifier 10.1109/JSTARS.2019.2940065

In practice, the stripes noise exhibit complex structures (see [10] and [11] for summarization of six typical stripes features). Particularly, the persistent feature describes whether or not stripes extend in a whole scan line, which makes stripes can be categorized into two classes: *integral* and *partial*. Although the integral stripes are the most common, the partial stripes can also be found in many images. For example, in specific thermal bands of MODIS images [12], stripes may appear with random lengths, which is mainly due to the unstable detector whose sensitivity varies in a part of the scan during the scanning process [6], [13]. Both integral and partial stripes significantly lower the images visual quality and limit the application of the subsequent processing. The goal of destriping is to improve the visual quality of multispectral images (MSIs) and benefit the subsequent processing tasks, such as image unmixing [14], [15], classification [16], [17], target detection [18], [19], and image fusion [20], [21].

Destriping methods can be roughly divided into two categories: single image-based destriping methods and multiple image-based destriping methods (including MSIs and hyperspectral images).

Single image-based methods generally fall into three classes: digit filtering-based methods, statistics-based methods, and optimization-based methods. Filtering-based methods suppress the stripes noise by constructing a filter on a transformed domain, such as Fourier transform [9], wavelet analysis [22], [23], and the combined domain filter [24], [25]. Statistics-based methods focus on the statistical properties of the digital numbers for each detector, such as moment matching [26] and histogram matching [27]. However, most of the above methods is not satisfactory when dealing with complex stripes cases, e.g., nonlinear, high density, and inclined direction, etc. Optimization-based methods regard stripes noise removal as an ill-posed inverse problem [11], [12], [28]–[37], and stabilize the original problem by introducing regularizations. For example, Bouali *et al.* [12] proposed a unidirectional variational (UV) model based on the directional signature of stripes. Chang *et al.* [38] introduced the low-rankness regularization to capture global redundancy of stripes. In [39], the authors proposed the group sparsity to reveal the sparsity of stripes in the group, and this group is always one column. Then, they proposed to minimize the $\ell_{2,1}$ -norm of stripes to promote its group sparsity.

Multiple image-based methods [6], [38], [40]–[46] perform destriping by exploiting the spatial and spectral regularizations of the latent image and stripes. One common spatial regularization is total variational (TV), which depicts the piecewise

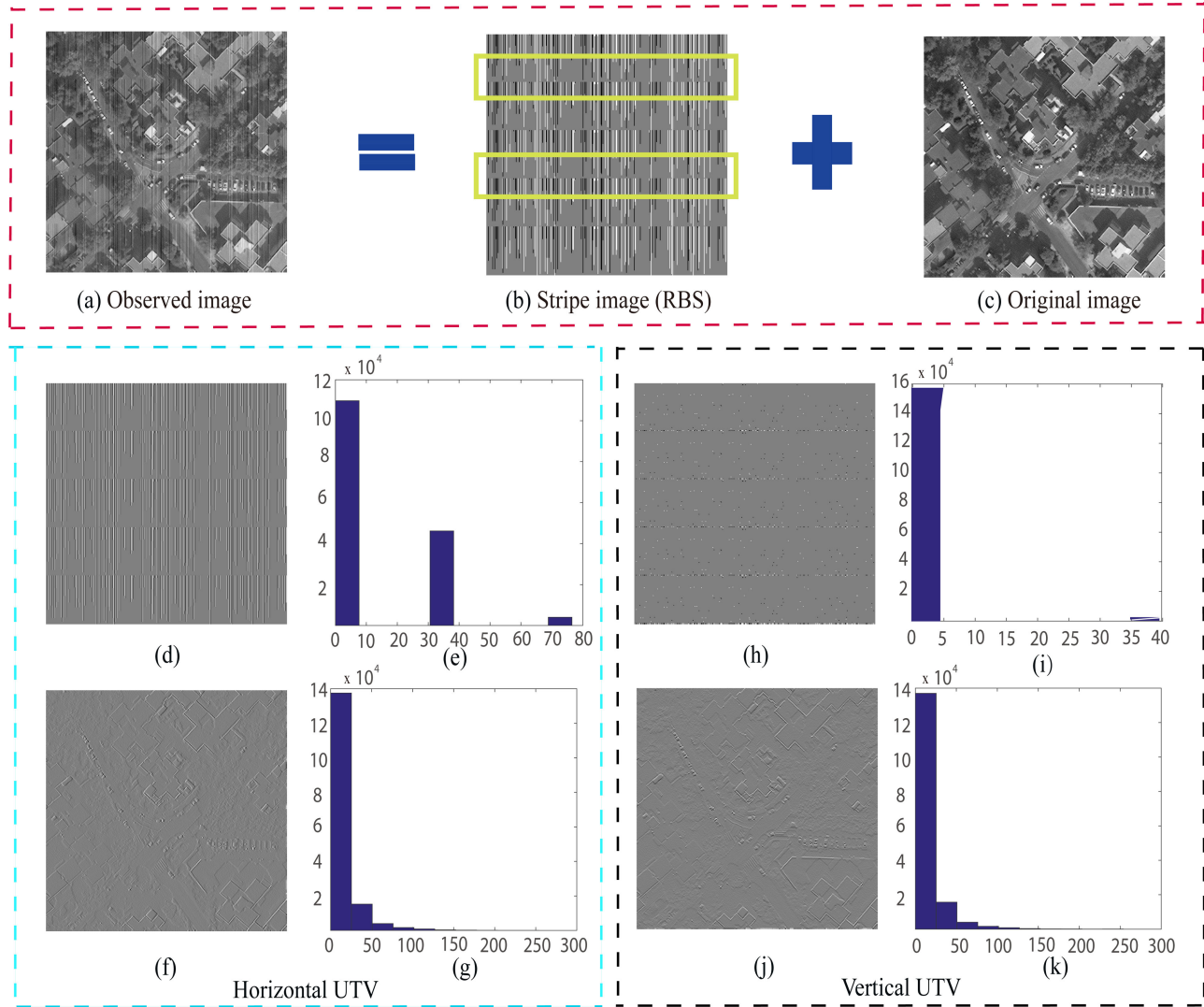


Fig. 1. Overview of the proposed method. (a) Observed image. (b) Stripe image. (c) Original image. (d)–(g) Horizontal derivative images of (b) and (c), and the corresponding histograms. (h)–(k) Vertical derivative images of (b) and (c), and the corresponding histograms.

smooth of the target MSIs in the spatial dimension [42], [43], [47], [48]; while the spectral regularization is often characterized by (matrix) low-rankness, which describes the spectral perspective in a low-rank subspace [6], [44], [49]. However, these methods ignore the regularizations of the stripe layer. Thus, Chang *et al.* proposed [38] to simultaneously consider the piecewise smoothness of the target image and the low-rankness of stripes. Recently, the tensor low-rankness regularization has gotten extensive attention [45], which has effectively utilized the tensor structure of MSIs.

Low rankness assumes that the stripes have the global redundancy and the group sparsity assumes the sparsity of stripes in the group (this group is always one column). The above methods perform well when the stripes satisfy the corresponding assumptions, however, in real scenarios, the stripes are very complex and these assumptions are always violated. Motivated by this, we need to find a more flexible regularization to describe the complex stripes. We divide the stripe layer into several blocks

along the stripe-perpendicular direction, then we use group sparsity to characterize the sparsity of each block, which can more flexibly control group size. Further, we observe that stripes are nonuniform and $\ell_{2,1}$ -norm cannot effectively promote the group sparsity of the solution in many cases [50]–[52]. Thus, we propose a reweighted $\ell_{2,1}$ -norm regularization to characterize the intrinsic structure of stripes.

Motivated by these observations, we propose a novel and flexible regularization, named as reweighted block sparsity (RBS), to better depict stripes and improve flexibility in dealing with real scenario, which by updating weight to adaptively controlling the sparsity level of the columns within each block. Moreover, we develop an adaptive updating strategy. Detailed modeling of this article can be found in Section II-A and Fig. 1. Alternating direction method of multipliers (ADMM) [53] is developed to solve the proposed model efficiently. Experimental results demonstrate that the proposed method achieves better despeckling performance than the state-of-the-art competitors. In addition, it

is clear that a single image destriping is more challenging, since it only relies on the prior information of a single image. Thus, this article focuses on a single image destriping, and our method can be extended to multiple image destriping easily.

The main contributions of this article are summarized as follows.

We propose a novel and flexible RBS regularization to characterize the block sparsity of stripes, which can flexibly handle the complex stripes, e.g., the partial stripes.

- 1) Based on RBS, we propose a novel destriping model by integrating RBS and unidirectional total variation (UTV) regularization.
- 2) We develop an ADMM algorithm to solve the proposed model.

The rest of this article is organized as follows. Section II gives the proposed model and its optimization procedure. Section III gives experimental results and discussion. Finally, we conclude this article in Section IV.

II. PROPOSED METHOD

This section is divided into two parts. Section II-A gives the proposed model and analyzes the motivation of each term. Section II-B develops an effective ADMM-based [53] algorithm to solving the proposed model.

A. Proposed Model

We consider the following degradation model [38]:

$$Y = U + S$$

where Y , U , and $S \in \mathbb{R}^{m \times n}$ represent the observed image, the original image, and the stripe component, respectively. In this article, we consider every stripe is vertical. If stripes are horizontal, we can rotate them to make the stripes vertical. The proposed destriping model is as follows:

$$\arg \min_S \|\nabla_y S\|_{1,1} + \lambda_1 \sum_{i=1}^s \|S_i\|_{w,2,1} + \lambda_2 \|\nabla_x(Y - S)\|_{1,1} \quad (1)$$

where the first two terms are the vertical UTV and RBS regularization of stripes, respectively, and the third term is the horizontal UTV regularization of the desired image. Here, ∇_x and ∇_y are the horizontal and vertical differential operators, respectively, $\|\cdot\|_{1,1}$ represents the sum of the absolute values of all elements, and λ_i ($i = 1, 2$) are positive regularization parameters to balance the three terms.

We give the details of RBS regularization. We partition S into s blocks $[S_1^T, \dots, S_s^T]^T$, where $S_i \in \mathbb{R}^{d_i \times n}$ (for $i = 1, \dots, s$) denotes the i th block, $\sum_{i=1}^s d_i = m$, and the positive integer $s \in [1, m]$ controls the block number. The weighted $\ell_{2,1}$ norm of S_i is defined as

$$\|S_i\|_{w,2,1} = \sum_{j=1}^n w_{i,j} \|S_i^{[j]}\|_2$$

where $S_i^{[j]}$ is the j th column of the i th block of S , $w = [w_{i,j}]_{s \times n}$ is a nonnegative weighting matrix, and $w_{i,j} = \frac{1}{\|S_i^{[j]}\|_2 + \epsilon}$ for $i = 1, \dots, s, j = 1, \dots, n$, ϵ is set to 10^{-16} to avoid dividing by zero. It is clear that if $s = m$, correspondently, $d_1 = \dots = d_i = 1$, each group-sparse row block reduces to a sparse vector and the block sparsity reduces to the global ℓ_1 norm; whereas if $s = 1$, correspondently, $d_1 = m$, then there is only one block, and the block sparsity reduces to group sparsity. Below we give the motivation for each regularization term.

1) RBS Regularization of the Stripe Layer: We use RBS regularization to characterize the partial-group-sparse structure of stripes. To illustrate our motivation, we first partition S to several row blocks [54], then we observe that stripes of each block are group sparse in Fig. 1(b). In order to promote the group sparsity of each block, we introduce the weight w to adaptively control the penalization level. We develop an adaptive strategy for the update of w . In the perspective of sparse optimization, we set w inversely proportional to $\|S_i^{[j]}\|_2$, to approximate the $\ell_{2,0}$ -regularization, we have $\|S\|_{w,2,1} = \|S\|_{2,0}$ [50]–[52]. Based on the above discussion, we use $\sum_{i=1}^s \|S_i\|_{w,2,1}$ to explore the partial-group-sparse structural of the stripe layer.

2) Horizontal UTV Regularization of the Image Layer: We use the horizontal UTV regularization to smooth the horizontal derivative of the image layer. Fig. 1(d) and (f) is horizontal derivative images of the stripe layer and the image layer, the corresponding histograms as shown in (e) and (g), respectively. These subfigures reveal that the horizontal derivative of the image layer is much sparser than the stripe layer. Based on these observations, we use $\|\nabla_x(Y - S)\|_{1,1}$ to preserve the sharp edges and the piecewise smoothness of the image layer.

3) Vertical UTV Regularization of the Stripe Layer: We use the vertical UTV regularization to characterize the direction characteristic of the stripe layer. Fig. 1(h) and (j) shows the vertical derivative images of the stripe layer and the image layer, the corresponding histograms as shown in (g) and (k), respectively. From these subfigures, we observe that the vertical derivative is quite sparse. Therefore, we use $\|\nabla_y S\|_{1,1}$ as the regularization term of the stripe layer.

B. ADMM Optimization Algorithm

In this section, we adopt an ADMM [53] algorithm to solving the proposed model (1).

We introduce three auxiliary variables $D = \nabla_y S$, $Q = S$, and $V = \nabla_x(Y - S)$, and partition $Q = [Q_1^T, \dots, Q_s^T]^T$, then (1) is equivalent to the following constrained problem:

$$\begin{aligned} & \arg \min_{S,D,Q,V} \|D\|_{1,1} + \lambda_1 \sum_{i=1}^s \|Q_i\|_{w,2,1} + \lambda_2 \|V\|_{1,1} \\ & \text{s.t. } D = \nabla_y S, \quad Q = S, \quad V = \nabla_x(Y - S) \end{aligned} \quad (2)$$

where $\|Q_i\|_{w,2,1} = \sum_{j=1}^n w_{i,j} \|Q_i^{[j]}\|_2$, and $w_{i,j} = \frac{1}{\|Q_i^{[j]}\|_2 + \epsilon}$.

The augmented Lagrangian function of (2) is given by

$$\begin{aligned} L(D, Q, V, S, P_1, P_2, P_3) = & \|D\|_{1,1} + \frac{\beta}{2} \left\| \nabla_y S - D + \frac{P_1}{\beta} \right\|_F^2 \\ & + \lambda_1 \sum_{i=1}^s \|Q_i\|_{w,2,1} + \frac{\beta}{2} \left\| S - Q + \frac{P_2}{\beta} \right\|_F^2 \\ & + \lambda_2 \|V\|_{1,1} + \frac{\beta}{2} \left\| \nabla_x(Y - S) - V + \frac{P_3}{\beta} \right\|_F^2 \end{aligned}$$

where P_1 , P_2 , and P_3 denote the Lagrange multipliers and β is positive penalty parameter. Then, ADMM iterates as follows:

$$\begin{cases} (D^{l+1}, Q^{l+1}, V^{l+1}) = \arg \min_{D, Q, V} L(S^l, D, Q, V, P_1^l, P_2^l, P_3^l) \\ S^{l+1} = \arg \min_S L(S, D^{l+1}, Q^{l+1}, V^{l+1}, P_1^l, P_2^l, P_3^l) \\ P_1^{l+1} = P_1^l + \beta(\nabla_y S^{l+1} - D^{l+1}) \\ P_2^{l+1} = P_2^l + \beta(S^{l+1} - Q^{l+1}) \\ P_3^{l+1} = P_3^l + \beta(\nabla_x Y - \nabla_x S^{l+1} - V^{l+1}). \end{cases}$$

Below we give the details of solving each subproblem.

- 1) In step 1, since the variables D , Q , and V are decoupled, their optimal solutions can be calculated separately.

a) The D -subproblem is

$$D^{l+1} = \arg \min_D \|D\|_{1,1} + \frac{\beta}{2} \left\| \nabla_y S^l - D + \frac{P_1^l}{\beta} \right\|_F^2$$

which can be efficiently solved by the following soft-threshold shrinkage operation [55], [56]:

$$D^{l+1} = \text{shrink} \left(\nabla_y S^l + \frac{P_1^l}{\beta}, \frac{1}{\beta} \right) \quad (3)$$

where

$$(\text{shrink}(A, b))_{i,j} = \text{sign}(A_{i,j}) * \max(|A_{i,j}| - b, 0)$$

and the convention $0 \cdot 0$ is assumed.

b) The Q -subproblem is

$$\begin{aligned} Q^{l+1} = & \arg \min_Q \lambda_1 \sum_{i=1}^s \|Q_i\|_{w,2,1} \\ & + \frac{\beta}{2} \left\| S^l - Q + \frac{P_2^l}{\beta} \right\|_F^2. \end{aligned}$$

Let $S = [S_1^T, \dots, S_s^T]^T$ and $Q = [Q_1^T, \dots, Q_s^T]^T$, we correspondently partition $P_2 = [P_{2,1}^T, \dots, P_{2,s}^T]^T$. Then, we obtain the j th column of the i th block of Q^{l+1} by the following soft-shrinkage formula [54]:

$$(Q_i^{[j]})^{l+1} = \max \left(\|r_{i,j}\|_2 - \frac{\lambda_1 w_{i,j}}{\beta}, 0 \right) \frac{r_{i,j}}{\|r_{i,j}\|_2} \quad (4)$$

$$\text{where } r_{i,j} = (S_i^{[j]})^l + \frac{1}{\beta} (P_{2,i}^{[j]})^l \quad \text{and} \quad w_{i,j} = \frac{1}{\|(S_i^{[j]})^l\|_2 + \epsilon}.$$

Algorithm 1: The RBS Destriping Algorithm.

Input: Observed image Y , parameters $\lambda_1, \lambda_2, \beta$.
Initialize: $S^1 = D^1 = Q^1 = V^1 = P_1^1 = P_2^1 = P_3^1 = 0$, $S^0 = Y$, $\varepsilon = 10^{-4}$, and maxiter = 1000, $l = 0$.
1: **While** ($\|S^{l+1} - S^l\|_F / \|S^l\|_F > \varepsilon$ and $k \leq \text{maxiter}$)
2: $l = l + 1$;
3: $w_{i,j} = \frac{1}{\|(S_i^{[j]})^l\|_2 + \epsilon}$;
4: Update D^{l+1} , Q^{l+1} , and V^{l+1} via (3), (4), and (5);
5: Update S^{l+1} via (6);
6: Update the multiplier P_1^{l+1} , P_2^{l+1} , and P_3^{l+1} via (7);
7: **End while**
8: Restored image $U = Y - S^{l+1}$.

Output: Restored image U and the stripe noise S^{l+1} .

c) The V -subproblem is

$$V^{l+1} = \arg \min_V \lambda_2 \|V\|_{1,1}$$

$$+ \frac{\beta}{2} \left\| \nabla_x(Y - S^l) - V + \frac{P_3^l}{\beta} \right\|_F^2$$

which can be similarly solved as

$$V^{l+1} = \text{shrink} \left(\nabla_x(Y - S^l) + \frac{P_3^l}{\beta}, \frac{\lambda_2}{\beta} \right). \quad (5)$$

- 2) In step 2, the S -subproblem is a least square problem [57] given by

$$\begin{aligned} S^{l+1} = & \arg \min_S \frac{\beta}{2} \left\| \nabla_y S - D + \frac{P_1^l}{\beta} \right\|_F^2 \\ & + \frac{\beta}{2} \left\| S - Q + \frac{P_2^l}{\beta} \right\|_F^2 \\ & + \frac{\beta}{2} \left\| \nabla_x(Y - S) - V + \frac{P_3^l}{\beta} \right\|_F^2 \end{aligned}$$

and the corresponding solution can be obtained by solving the normal equation as follows:

$$\begin{aligned} (\nabla_y^T \nabla_y + I + \nabla_x^T \nabla_x) S = & \nabla_y^T \left(D^{l+1} - \frac{P_1^l}{\beta} \right) \\ & + \left(Q^{l+1} - \frac{P_2^l}{\beta} \right) + \nabla_x^T \left(\nabla_x Y - V^{l+1} + \frac{P_3^l}{\beta} \right) \end{aligned} \quad (6)$$

the normal equation can be solved by using Fast Fourier Transform.

- 3) In step 3, we update the Lagrange multipliers P_1 , P_2 , and P_3 as follows:

$$\begin{cases} P_1^{l+1} = P_1^l + \beta(\nabla_y S^{l+1} - D^{l+1}) \\ P_2^{l+1} = P_2^l + \beta(S^{l+1} - Q^{l+1}) \\ P_3^{l+1} = P_3^l + \beta(\nabla_x Y - \nabla_x S^{l+1} - V^{l+1}). \end{cases} \quad (7)$$

The whole ADMM iterative scheme for the model (1) is outlined in Algorithm 1.

III. EXPERIMENTAL RESULTS AND DISCUSSION

In this section, we give experimental results to test the performance of the proposed method. Section III-A gives the experimental settings. Section III-B and III-C test the proposed method using simulated and real data, respectively. Some discussions are given in Section III-D.

A. Experimental Setting

For single image destriping, we compare the proposed method (denoted as RBSUTV) with three state-of-the-art methods: the unidirectional variation model [12] (denoted as UV), the low-rank-based single-image decomposition model [38] (denoted as LRSID), and TV regularization and group sparsity constraint method [58] (denoted as UTVGS). For multiple images destriping, we compare the proposed method with the anisotropic spectral-spatial TV model [43] (denoted as ASSTV), the image decomposition based band-by-band low-rank regularization and spatial-spectral TV model [38] (denoted as LRMID), and the low-rank tensor decomposition model [45] (denoted as LRTD). All experiments are conducted under Windows 10 and MATLAB R2016b running on a desktop with an Intel(R) Core (TM) i5-4590 CPU @ 3.30 GHz and 16 GB memory.

1) *Stripes Noise Generation*: In our experiment, all the data are in radiance and we normalize the data between [0, 1] for a fair comparison. We denote the stripes level using a vector with two elements, e.g., (intensity and percentage), where “intensity (denotes as I)” denotes the absolute values of pixels of stripes and “percentage (denotes as r)” represents the percentage of the stripes area within the image. In our simulated experiments, I is {0.5, 0.8}, and r is {0.2, 0.5, 0.8}. We randomly select $r \times n$ columns of the image to add stripes. For both integral and partial cases, the absolute values of each pixel of each stripe column take the same. In particular, for the partial stripes case, the lengths of each stripe are randomly distributed on the image.

2) *Evaluation Indices*: We use several qualitative and quantitative assessments to evaluate the destriping performance. Mean cross-track profile is a table, where the x -axis stands for the column number of images and the y -axis represents the mean value of each column.

For a single image, the peak signal-to-noise ratio [59] (PSNR) and the structural similarity index [60] (SSIM) are defined as follows:

$$\text{PSNR} = 10 \log_{10} \frac{mn(\text{Max}_U)^2}{\|U - U^*\|_F^2}$$

$$\text{SSIM} = \frac{(2\mu_U \cdot \mu_{U^*} + c_1)(2\sigma_{UU^*} + c_2)}{(\mu_U^2 + \mu_{U^*}^2 + c_1)(\sigma_U^2 + \sigma_{U^*}^2 + c_2)}$$

where U is the destriped image, U^* is the original image, Max_U is the maximum pixel of U , μ_U and μ_{U^*} are the mean values of U and U^* , respectively, σ_{UU^*} is the covariance of U and U^* , σ_U and σ_{U^*} are the standard variances of U and U^* , respectively, and $c_1, c_2 > 0$ are constants. For the multiple images, the quality of the destriped image is measured by the average of PSNR, SSIM, and the mean spectral angle mapper [61] (MSAM), which is

defined as follows:

$$\text{MSAM} = \frac{1}{mn} \sum_{i=1}^{mn} \arccos \frac{(\mathcal{U}^i)^T \cdot (\mathcal{U}^{*i})}{\|\mathcal{U}^i\| \cdot \|\mathcal{U}^{*i}\|}$$

where \mathcal{U}^i and \mathcal{U}^{*i} are the i th spectral signatures of the ground-truth and the destriped multiple image, respectively. In general, higher PSNR, SSIM values, and smaller MSAM imply better destriping results. For the real experiments, we choose no-reference evaluation indices mean relative deviation [6], [8], [12] (MRD) to evaluate the performance of the proposed method, since the ground-truth images are unavailable. In this article, we used noise reduction (NR) [6], [12], [62] to evaluate the destriping quality when stripes are periodic, since the power spectrum of periodic stripes exhibits clear peaks.

These indices are defined as follows:

$$\text{NR} = \frac{N_0}{N_1}$$

$$\text{MRD} = \frac{1}{mn} \sum_{i=1}^{mn} \frac{|x_i - y_i|}{y_i} \times 100\%$$

where N_0 is the power of the frequency component of the destriped image, N_1 is the power of the frequency component of the observed image, x_i is the pixel value of the destriped image, and y_i is the pixel value of the observed image. It is noteworthy that higher NR values and lower MRD values usually mean better destriping results.

3) *Parameter Setting*: Our method involves the four parameters: λ_i ($i = 1, 2$), β , and s in model (1). The parameters λ_1 and λ_2 balance the relative weight of the regularization terms, and we set them in the range of [0.001, 1]. The penalty parameter β controls the speed of convergence and is chosen as 1 in our model. The parameter s controls the number of blocks, and it is largely determined by the number of rows per block (denotes as d). We will discuss the selections of λ_1 , λ_2 , and s in Section III-C. Parameters in the compared methods are set as the suggested values in the references.

B. Simulated Experiments

In the simulated experiments, we test the proposed method on partial and integral stripes. The IKONOS image¹ with size 400×400 , the MODIS images² with size 400×400 , and the Washington DC Mall³ are used as testing images. The original Washington DC Mall contains 191 spectral bands with 1208×307 pixels in each band, and we extract a subimage with size $256 \times 256 \times 11$ in our experiments.

1) *Partial Stripe Case*: The first row of Fig. 2 displays the destriped results by different methods on the partial stripes case using the IKONOS image with $r = 0.5$ and $I = 0.2$. In Fig. 2, we observe that LRSID blurs the boundaries causing the details loss. UV and UTVGS contain a small number of stripes in the residual maps. It is clear that our method erases stripes and remains original image details better. In addition, we also

¹<https://openremotesensing.net/>

²<https://ladsweb.nascom.nasa.gov/>

³<https://engineering.purdue.edu/biehl/MultiSpec/hyperspectral.html>

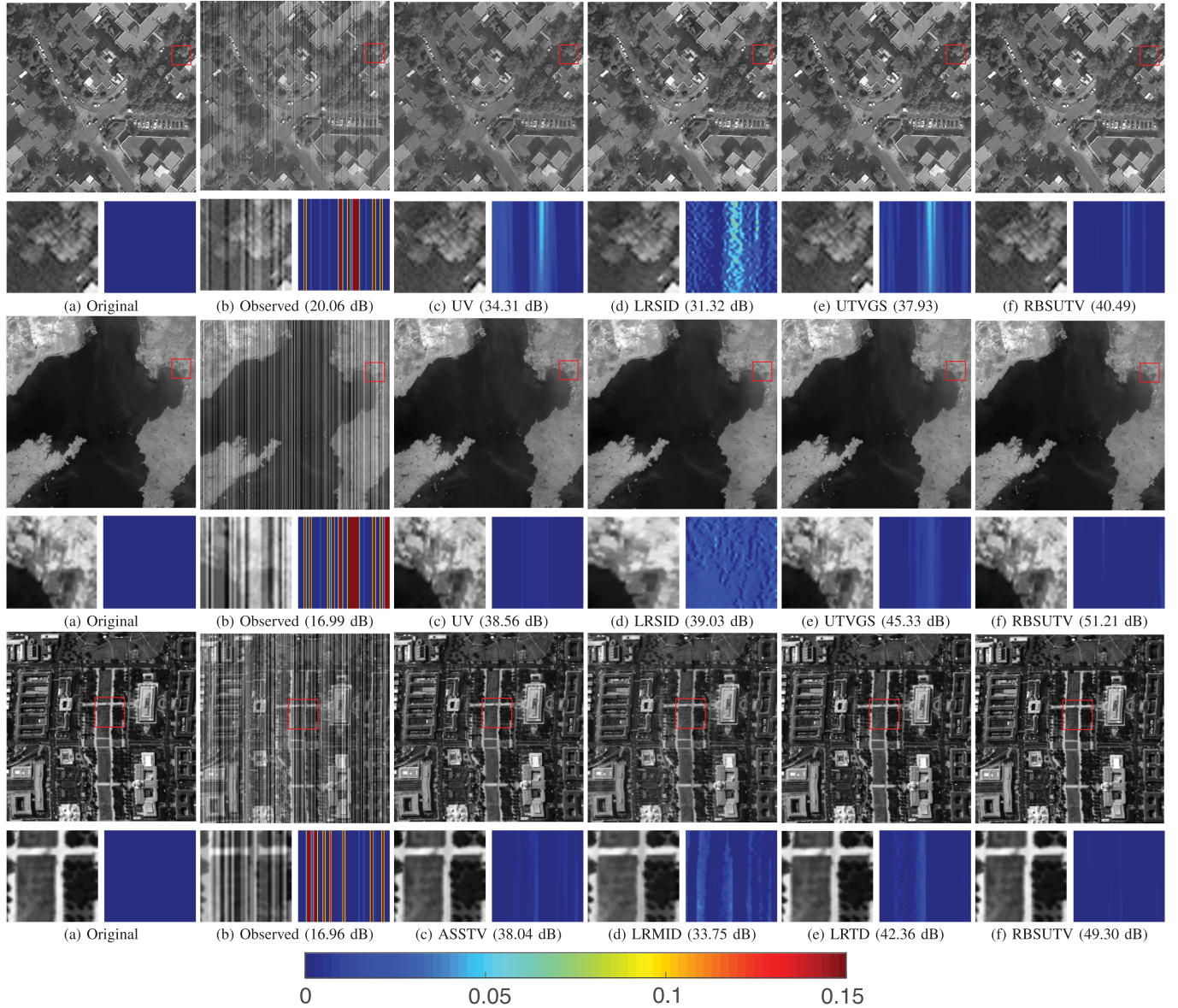


Fig. 2. Destriping results, the magnified results of the selected area (left), and the corresponding residual maps (right) (each value in parentheses represents the corresponding PSNR value). (a) The original images. (b) Observed images. (c)–(f) Destriped results by the different methods. From top to bottom: band 36 of IKONOS, band 32 of Aqua MODIS, and band 3 of Washington DC Mall, respectively.

enlarge the selected area and show the corresponding residual maps (the difference between destriped images and original images) in Fig. 2. We can see that the residual maps by the three comparative methods show some residual stripes. They fail to precisely estimate the stripes and create some minor errors in the stripe-free regions. As a comparison, the destriped results extracted by the proposed method are the closest to the original images.

Fig. 3 shows the column mean cross-track profiles of Fig. 2. In Fig. 3, we observe that the curves of the proposed method is closer to the original curves than that of the comparative methods, which is consistent with the visual results.

2) *Integral Stripe Case*: The proposed model is also applicable for the integral stripes or MSIs by incorporating the TV regularization along the spectral dimension. The second

row and third row of Fig. 2 show the destriped results by the different methods using band 32 of Aqua MODIS with $r = 0.5$ and $I = 0.2$, and the Washington DC Mall with $r = 0.5$ and $I = 0.2$. The corresponding column mean cross-track profiles comparison as shown in Fig. 3. Fig. 4 shows the PSNR and SSIM values of each band of the destriped results. We observe that the PSNR and SSIM values of the proposed method are significantly higher than those of the compared methods in all bands.

Tables I and II show the PSNR (dB), SSIM, and MSAM values in terms of all simulated experiments under different noise levels. We observe that the proposed method obtains better PSNR, SSIM, and MSAM values in the simulated experiments. In summary, the quantitative comparison is in accordance with the visual results presented in the above.

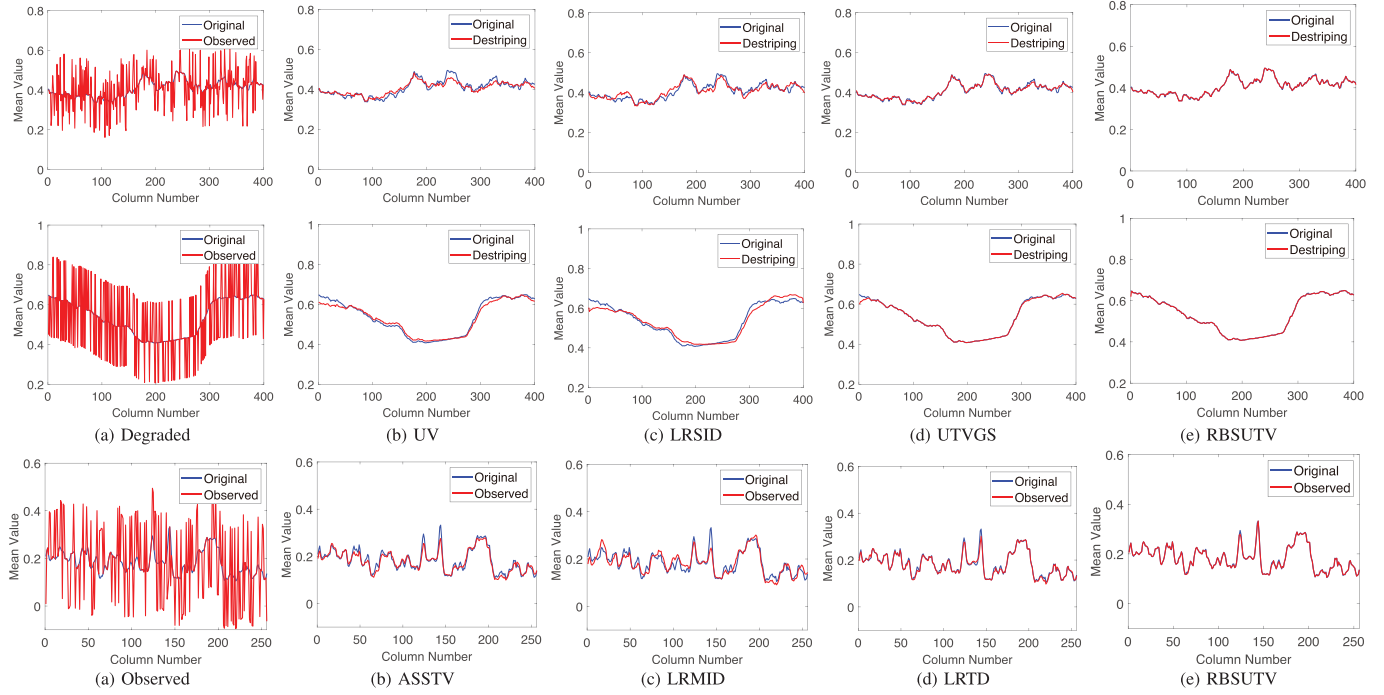


Fig. 3. Column mean cross-track profiles of Fig. 2. (a) Column mean cross-track profiles comparison between the original images and the observed images. (b)–(e) Column mean cross-track profiles comparison between the original images and the destriped images by the different methods.

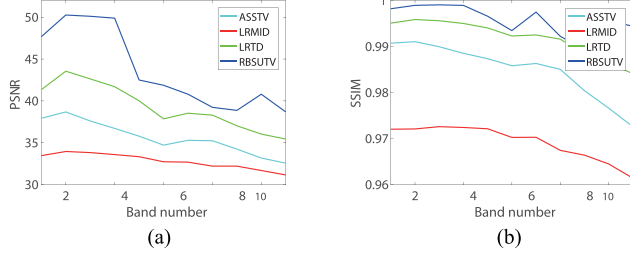


Fig. 4. PSNR and SSIM values of each band for Washington DC Mall. (a) PSNR values. (b) SSIM values.

C. Real Experiments

In this section, we test real data to illustrate the efficiency of the proposed method. In the real experiments, we select the band 24 of Aqua MODIS, band 27 of Terra MODIS, and band 33 of Aqua MODIS to test model (1). The Hyperion image⁴ was used in [43], and we conduct the experiment on whole Hyperion image after removing the atmosphere and water absorption bands. The size of the original image and the test image are $256 \times 256 \times 242$ and $256 \times 256 \times 155$, respectively.

Fig. 5 shows the destriped results by the different methods. Table III presents the MRD and NR evaluation results by the different methods. From Fig. 5, we can see that the comparative methods have some residual stripes and blur the observed images. We observe that UV can remove all stripes, but some regions are blurred. LRSID blurs the boundaries and many residual stripes still exist. UTVGS contains a bit of stripes. The proposed

method performs better than the other three competitive methods in terms of stripes removal and detail preservation. Table III indicates that the proposed method has better NR and MRD results than the compared destriping methods.

Fig. 6 shows the power spectrum curves of striped and destriped images of Fig. 5. The vertical and horizontal axes represent the normalized frequency and the mean power spectrum of all row, respectively. In Fig. 6(a), the curves of the observed images exist some peaks due to the existence of stripes. From Fig. 6(b)–(d), the sharp impulse of curves become smooth, but in the other positions, the mean power spectrum of the destriped images show most of the burrs compared with the observed image power spectrum one. Fig. 6(e), we can see that the power spectrum is closer to the curves of the observed images except for the peaks, which implies that our method can preserve details and remove stripes well because stripes correspond to the peaks. These curves are consistent with the above results of visual comparison.

D. Discussion

1) *Effect of the Block Size:* We discuss the influence of the block size. In our model, the parameter d controls the number of rows per block. Table IV lists the PSNR (dB) and SSIM values of the proposed method using $d = 1, 10, 20, 50, 200, 400$ with $r = 0.5$ and $I = 0.8$. We observe that medium d gets the best results. Therefore, we choose $d = 10$ to provide competitive quantitative evaluation results.

2) *Effect of Regularization Terms:* We test the effects of the two regularization terms of stripes, i.e., the RBS and UTV. Fig. 7 shows different settings of regularization terms using

⁴<http://compression.jpl.nasa.gov/hyperspectral/imagedata/>

TABLE I
PSNR AND SSIM RESULTS BY THE DIFFERENT METHODS ON DIFFERENT STRIPES NOISE

case	r	I	Index	Degradate	UV	LRSID	UTVGS	RBSUTV
partial	0.5	0.2	PSNR	20.06	34.31	31.32	37.93	40.49
			SSIM	0.732	0.989	0.967	0.993	0.997
		0.5	PSNR	12.10	30.41	26.17	35.92	38.25
			SSIM	0.434	0.985	0.911	0.993	0.995
			PSNR	8.02	27.19	23.67	35.18	36.88
	0.8	0.8	SSIM	0.300	0.979	0.854	0.993	0.994
		0.5	PSNR	18.08	30.38	28.67	32.89	34.91
			SSIM	0.664	0.980	0.959	0.985	0.990
			PSNR	10.12	25.79	23.98	30.85	34.17
			SSIM	0.347	0.966	0.877	0.982	0.987
	0.8	0.8	PSNR	6.036	22.48	21.47	29.90	34.03
		SSIM	0.218	0.948	0.794	0.982	0.987	
		0.5	PSNR	16.99	38.56	39.03	45.33	51.21
			SSIM	0.255	0.999	0.999	0.999	0.999
			PSNR	9.03	37.12	37.56	46.35	51.37
			SSIM	0.066	0.998	0.999	0.999	0.999
			PSNR	4.95	33.21	33.04	47.15	51.43
integral	0.8	0.8	SSIM	0.028	0.994	0.996	0.999	0.999
		0.5	PSNR	14.95	37.36	38.24	36.55	50.43
			SSIM	0.205	0.999	0.998	0.998	0.999
			PSNR	6.99	30.53	30.25	37.04	50.71
			SSIM	0.049	0.995	0.997	0.998	0.999
	0.8	0.8	PSNR	2.91	25.91	26.27	38.02	50.63
		SSIM	0.019	0.985	0.992	0.998	0.999	

*The best values are highlighted in bold.

TABLE II
PSNR, SSIM, AND MSAM RESULTS BY THE DIFFERENT METHODS ON DIFFERENT STRIPES NOISE

case	r	I	Index	Degradate	UV	LRMID	UTVGS	RBSUTV
MSIs	0.5	0.2	PSNR	16.96	38.04	39.07	42.36	49.30
			SSIM	0.354	0.985	0.991	0.992	0.993
		0.5	MSAM	0.752	0.075	0.995	0.058	0.030
			PSNR	9.00	31.96	32.65	42.76	48.24
			SSIM	0.081	0.968	0.975	0.993	0.997
	0.8	0.5	MSAM	1.127	0.083	0.062	0.052	0.026
			PSNR	4.91	26.97	28.33	42.23	51.36
		0.8	SSIM	0.031	0.918	0.975	0.990	0.994
			MSAM	1.269	0.140	0.995	0.123	0.029
			PSNR	14.91	38.41	39.78	38.90	41.63
	0.8	0.2	SSIM	0.236	0.986	0.975	0.985	0.990
		0.5	MSAM	0.867	0.074	0.073	0.072	0.068
			PSNR	6.95	31.78	33.21	38.06	42.12
			SSIM	0.031	0.965	0.972	0.983	0.992
		0.8	MSAM	1.214	0.087	0.079	0.074	0.048
			PSNR	2.87	26.71	28.53	35.95	43.26
		0.8	SSIM	0.008	0.892	0.923	0.971	0.992
		0.8	MSAM	1.337	0.166	0.121	0.077	0.045

*The best values are highlighted in bold.

band 32 of Aqua MODIS as the testing image. Considering the residual maps (the difference with the original image and the destriped image), we observe that Fig. 7(h) contains less residual stripes than Fig. 7(f) and (g), which demonstrates that each regularization term contributes to the effect of the solution, and they are complementary and indispensable.

3) *Regularization Parameters λ_1 and λ_2 :* We discuss the effects of parameters λ_1 and λ_2 . To show their effects on the

destriping performance, we give an analysis by using a simulated partial experiment (IKONOS with $r = 0.5$ and $I = 0.2$). Fig. 8 shows the corresponding PSNR and SSIM indexes for different λ_1 and λ_2 values. Fig. 8 indicates that these two parameters have a great effect on the destriping performance. The parameters λ_1 and λ_2 control the relative weights of the regularization terms for stripes and the original image, respectively. In our experiments, we empirically set the parameter with the range [0.005, 0.025]

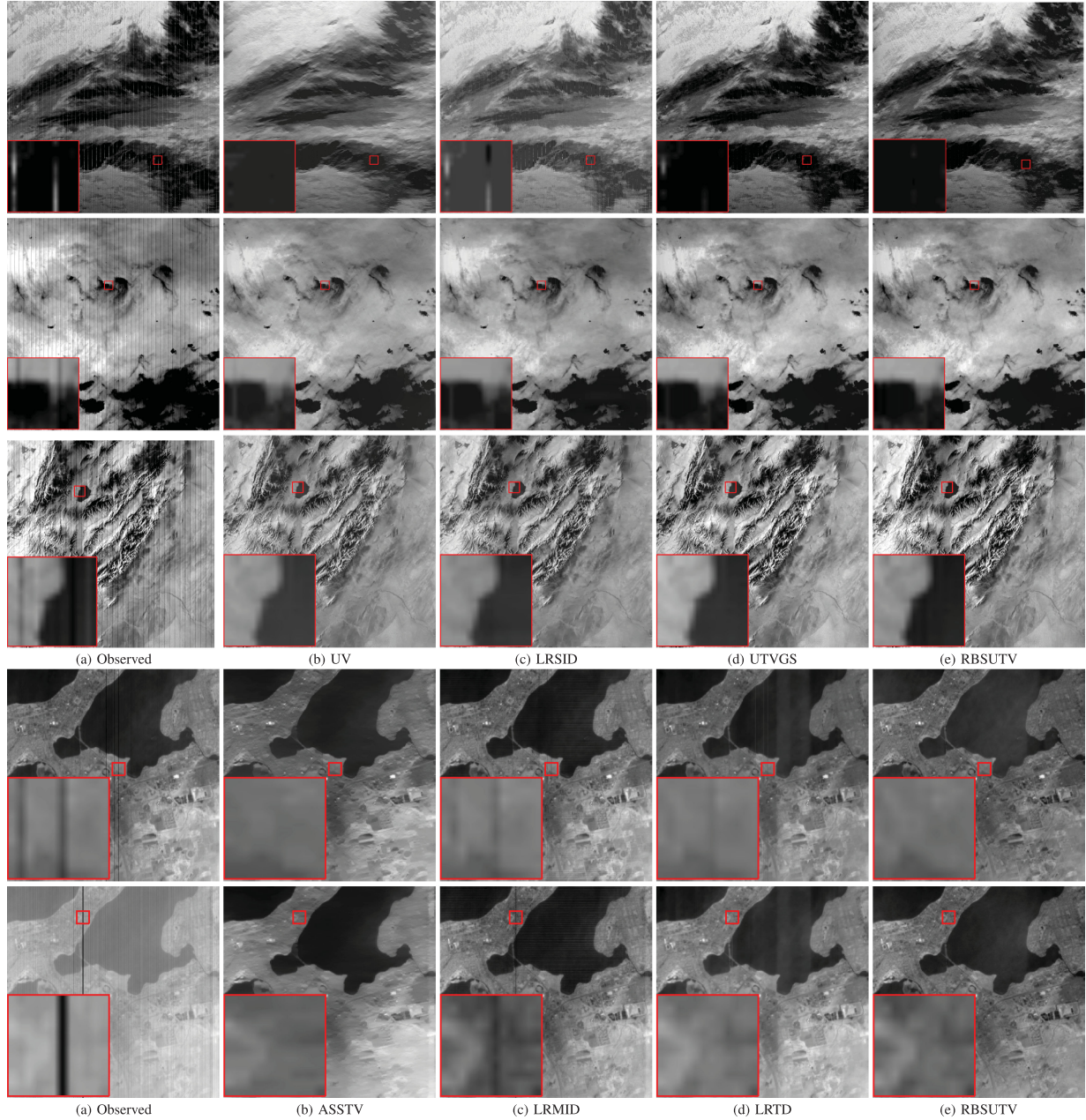


Fig. 5. Destriped results on real data. From top to bottom: band 24 of Aqua MODIS, band 27 of Terra MODIS, band 33 of Aqua MODIS, and band 33, and band 63 of the Hyperion image, respectively. (a) Observed. (b) ASSTV. (c) LRMID. (d) LRTD. (e) RBSUTV.

TABLE III
NR AND MRD VALUES OF THE TESTED METHODS FOR
THE REAL EXPERIMENTS

	Index	UV	LRSID	UTVGS	RBSUTV
MODIS band 24	NR	4.07	2.06	2.16	2.53
	MRD	0.047	0.022	0.026	0.036
MODIS band 27	NR	3.84	3.35	3.99	3.78
	MRD	0.167	0.062	0.064	0.054
MODIS band 33	NR	3.47	3.41	3.41	3.62
	MRD	0.045	0.047	0.035	0.035

for λ_1 and [0.005, 0.05] for λ_2 with an increment of 0.001 for all the experiments.

4) *Multiplicative Model*: There exist many models for simulating striping noise, e.g., the additive model [12] and the multiplicative model [8]. This article mainly focuses on the basic additive model, which is widely studied in the work of destriping [6], [10], [11], [38], [43], [45]. Despite its simplicity, our model not only performs well in simulated experiments but also in real experiments. Moreover, the multiplicative model can be reduced to the additive one as follows:

The degradation model of multiplicative stripes in [62], i.e., $y_{x,y} = A_{x,y}u_{x,y} + B_{x,y}$, where $A_{x,y}$ and $B_{x,y}$ are the relative

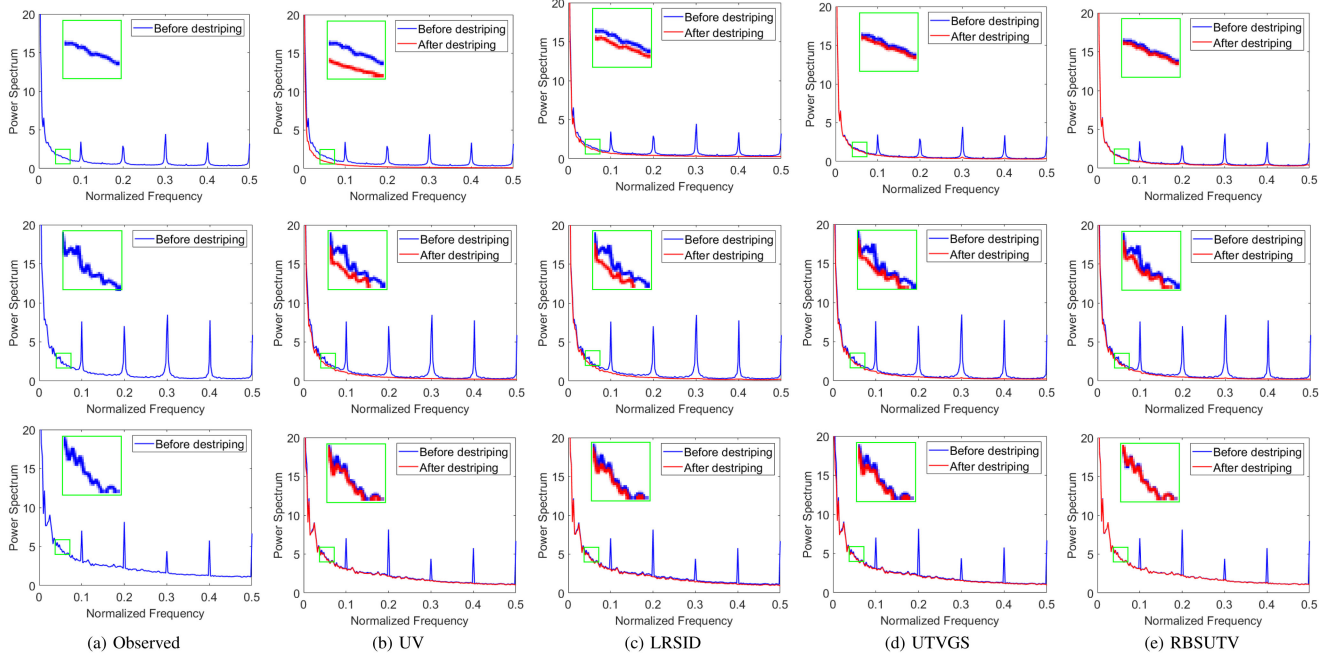


Fig. 6. Power spectrum curves of the striped and destriped images by different methods. From top to bottom: band 24 of Aqua MODIS, band 27 of Terra MODIS, and band 33 of Aqua MODIS, respectively.

TABLE IV

PERFORMANCE OF THE PROPOSED METHOD WITH DIFFERENT BLOCK SIZE

d	1	10	20	50	200	400
PSNR	36.63	36.88	36.37	35.92	35.61	35.52
SSIM	0.994	0.994	0.994	0.994	0.993	0.993

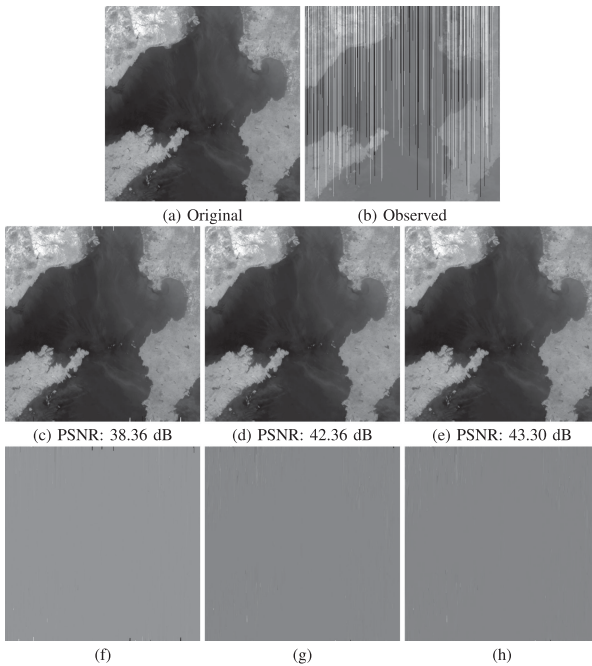


Fig. 7. (a) Original image. (b) Observed image. (c)–(d) Destriped results by the proposed method without the reweighted $\ell_{2,1}$ -regularization and without the vertical UTV regularization, respectively. (e) Proposed method. (f)–(h) Corresponding residual maps of (c)–(e).

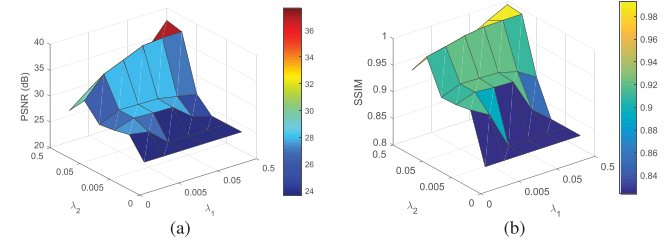


Fig. 8. (a) PSNR (dB) as a function of parameters λ_1 and λ_2 . (b) SSIM as a function of parameters λ_1 and λ_2 .

gain and offset parameters, respectively. The above model can be expressed in a matrix-vector form $Y = A \circ U + B$, where \circ denotes the element-wise multiplication. We rewrite the model as $Y = U + (A - 1_{m \times n}) \circ U + B$, where $1_{m \times n}$ is a matrix of all-ones and treat $(A - 1_{m \times n}) \circ U + B$ as additive noise.

Since the multiplicative model can be reduced to the additive model, we have conducted a simulated experiment with multiplicative stripes. First, we randomly choose $r \times n$ columns corrupted by multiplicative stripes, then for each contaminated column, entries of A and B take the same value randomly chosen from $[0, 1]$. We use band 32 of Aqua MODIS as the testing image. The destriping results and the corresponding residual maps (the difference between destriped image and original image) as shown in Fig. 9. Table V shows the PSNR and SSIM results by the different methods on band 32 of Aqua MODIS. These results suggest that our method can effectively remove the multiplicative stripes and exhibit superiority over the competing methods.

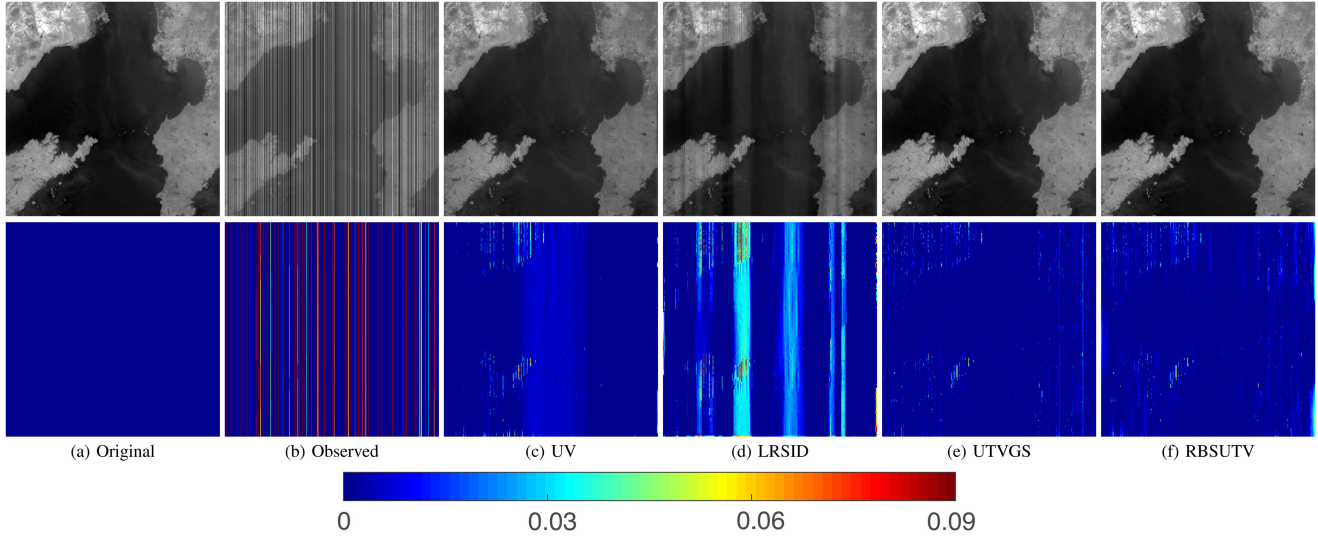


Fig. 9. (a) Original image. (b) Observed image. (c)–(f) Destriped results by the different methods. From top to bottom: The destriped results and the corresponding residual maps, respectively.

TABLE V
PSNR AND SSIM RESULTS BY THE DIFFERENT METHODS
ON BAND 32 OF AQUA MODIS

Index	Observed	UV	LRSID	UTVGS	RBSUTV
PSNR	13.89	31.55	28.85	41.72	44.90
SSIM	0.1388	0.9672	0.9765	0.9945	0.9971

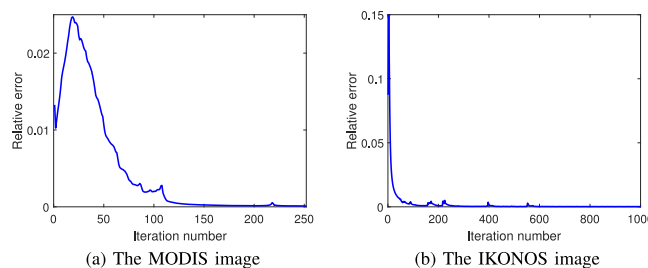


Fig. 10. Curves of relative error values versus iterations.

5) *Numerical Convergence of the Proposed Algorithm:* Due to the nonconvexity of the optimization problem, it is difficult to guarantee the convergence to a global minimum value theoretically. We test two images (the integral stripe case with $r = 0.5$ and $I = 0.2$ in the band 32 of MODIS, and the partial stripe case with $r = 0.5$ and $I = 0.2$ in the IKONOS image) to numerically illustrate the convergence of the proposed algorithm. Fig. 10 shows the relative error curves of the successive restored image S^l and S^{l+1} , i.e., $\|S^{l+1} - S^l\|_F / \|S^l\|_F$. From Fig. 10, we observe that the relative error keeps decreasing as the iteration number increases and our algorithm is convergent numerically.

IV. CONCLUSION

In this article, we propose a novel RBS regularization and a novel destriping model by combining RBS and UTV regularization. RBS partitions the stripe layer into several blocks along the stripe-perpendicular direction, and adapts that each block is group-sparse with an adaptive weight controlling the sparsity level, while UTV describes the local smoothness of the stripe layer. We develop an ADMM algorithm to solve the proposed model. Empirical studies on both synthetic and real-world data demonstrate the effectiveness of RBSUTV in comparison with the state-of-the-art methods.

ACKNOWLEDGMENT

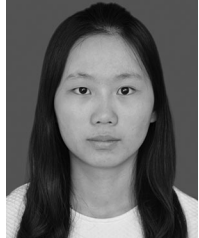
The authors would like to thank Dr. Y. Chang for sharing the Hyperion image and providing code for ASSTV and LRMID.

REFERENCES

- [1] J. A. Richards and X. Jia, *Remote Sensing Digital Image Analysis: An Introduction*, 4th ed. Berlin, Germany: Springer, 2006, pp. 343–380.
- [2] H. Shen, L. Huang, L. Zhang, P. Wu, and C. Zeng, “Long-term and fine-scale satellite monitoring of the urban heat island effect by the fusion of multi-temporal and multi-sensor remote sensed data: A 26-year case study of the city of Wuhan in China,” *Remote Sens. Environ.*, vol. 172, pp. 109–125, 2016.
- [3] M. Dees, B. Koch, C. Straub, Y. Wang, and H. Weinacker, “Airborne laser data for stand delineation and information extraction,” *Int. J. Remote Sens.*, vol. 30, no. 4, pp. 935–963, 2009.
- [4] X.-T. Li, X.-L. Zhao, T.-X. Jiang, Y.-B. Zheng, T.-Y. Ji, and T.-Z. Huang, “Low-rank tensor completion via combined non-local self-similarity and low-rank regularization,” *Neurocomputing*, to be published, doi: [10.1016/j.neucom.2019.07.092](https://doi.org/10.1016/j.neucom.2019.07.092).
- [5] M. Ding, T.-Z. Huang, T.-Y. Ji, X.-L. Zhao, and J.-H. Yang, “Low-rank tensor completion using matrix factorization based on tensor train rank and total variation,” *J. Sci. Comput.*, 2019, doi: [10.1007/s10915-019-01044-8](https://doi.org/10.1007/s10915-019-01044-8).
- [6] X. Lu, Y. Wang, and Y. Yuan, “Graph-regularized low-rank representation for destriping of hyperspectral images,” *IEEE Trans. Geosci. Remote Sens.*, vol. 51, no. 7, pp. 4009–4018, Jul. 2013.

- [7] Y. Zhang, G. Zhou, L. Yan, and T. Zhang, "A destriping algorithm based on TV-strokes and unidirectional total variation model," *Optik*, vol. 127, no. 1, pp. 428–439, 2016.
- [8] N. Acito, M. Diani, and G. Corsini, "Subspace-based striping noise reduction in hyperspectral images," *IEEE Trans. Geosci. Remote Sens.*, vol. 49, no. 4, pp. 1325–1342, Apr. 2011.
- [9] J. Chen, Y. Shao, H. Guo, W. Wang, and B. Zhu, "Destriping CMODIS data by power filtering," *IEEE Trans. Geosci. Remote Sens.*, vol. 41, no. 9, pp. 2119–2124, Sep. 2003.
- [10] X. Liu, H. Shen, Q. Yuan, X. Lu, and C. Zhou, "A universal destriping framework combining 1-D and 2-D variational optimization methods," *IEEE Trans. Geosci. Remote Sens.*, vol. 56, no. 2, pp. 808–822, Feb. 2018.
- [11] X. Liu, X. Lu, H. Shen, Q. Yuan, Y. Jiao, and L. Zhang, "Stripe noise separation and removal in remote sensing images by consideration of the global sparsity and local variational properties," *IEEE Trans. Geosci. Remote Sens.*, vol. 54, no. 5, pp. 3049–3060, May 2016.
- [12] M. Bouali and S. Ladjal, "Toward optimal destriping of MODIS data using a unidirectional variational model," *IEEE Trans. Geosci. Remote Sens.*, vol. 49, no. 8, pp. 2924–2935, Aug. 2011.
- [13] H.-S. Jung, J.-S. Won, M.-H. Kang, and Y.-W. Lee, "Detection and restoration of defective lines in the SPOT 4 SWIR band," *IEEE Trans. Image Process.*, vol. 19, no. 8, pp. 2143–2156, Aug. 2010.
- [14] M. D. Iordache, J. M. Bioucas-Dias, and A. Plaza, "Sparse unmixing of hyperspectral data," *IEEE Trans. Geosci. Remote Sens.*, vol. 49, no. 6, pp. 2014–2039, Jun. 2011.
- [15] N. Yokoya, X. Z. Xiao, and A. Plaza, "Multisensor coupled spectral unmixing for time-series analysis," *IEEE Trans. Geosci. Remote Sens.*, vol. 55, no. 5, pp. 2842–2857, Feb. 2017.
- [16] C. Yi, N. M. Nasrabadi, and T. D. Tran, "Hyperspectral image classification using dictionary-based sparse representation," *IEEE Trans. Geosci. Remote Sens.*, vol. 49, no. 10, pp. 3973–3985, Oct. 2011.
- [17] P. Ghamisi, M. D. Mura, and J. A. Benediktsson, "A survey on spectral-spatial classification techniques based on attribute profiles," *IEEE Trans. Geosci. Remote Sens.*, vol. 53, no. 5, pp. 2335–2353, May 2015.
- [18] S. K. Sinha and L. K. Tiwari, "Enhancement of image classification for forest encroachment mapping with destriped SWIR band in the wavelet domain," *IEEE J. Sel. Topics Appl. Earth Observ. Remote Sens.*, vol. 11, no. 7, pp. 2276–2281, Jul. 2018.
- [19] Q. Liu, L. Liu, and Y. Wang, "Unsupervised change detection for multispectral remote sensing images using random walks," *Remote Sens.*, vol. 9, no. 5, 2017, Art. no. 438.
- [20] N. Yokoya, C. Grohnfeldt, and J. Chanussot, "Hyperspectral and multispectral data fusion: A comparative review of the recent literature," *IEEE Trans. Geosci. Remote Sens.*, vol. 5, no. 2, pp. 29–56, Jun. 2017.
- [21] M. Joshi and A. Jalobeanu, "MAP estimation for multiresolution fusion in remotely sensed images using an IGMRF prior model," *IEEE Trans. Geosci. Remote Sens.*, vol. 48, no. 3, pp. 1245–1255, Mar. 2010.
- [22] J. Torres and S. O. Infante, "Wavelet analysis for the elimination of striping noise in satellite images," *Opt. Eng.*, vol. 40, no. 7, pp. 1309–1314, 2001.
- [23] J. Chen, H. Lin, Y. Shao, and L. Yang, "Oblique striping removal in remote sensing imagery based on wavelet transform," *Int. J. Remote Sens.*, vol. 27, no. 8, pp. 1717–1723, 2006.
- [24] B. Münch, P. Trtik, F. Marone, and M. Stampanoni, "Stripe and ring artifact removal with combined wavelet-Fourier filtering," *Opt. Express*, vol. 17, no. 10, pp. 8567–8591, 2009.
- [25] R. Pande-Chhetri and A. Abd-Elrahman, "De-striping hyperspectral imagery using wavelet transform and adaptive frequency domain filtering," *ISPRS J. Photogramm. Remote Sens.*, vol. 66, no. 5, pp. 620–636, 2011.
- [26] F. L. Gadallah, F. Csillag, and E. J. M. Smith, "Destriping multisensor imagery with moment matching," *Int. J. Remote Sens.*, vol. 21, no. 12, pp. 2505–2511, 2000.
- [27] B. K. P. Horn and R. J. Woodham, "Destriping Landsat MSS images by histogram modification," *Comput. Graph. Image Process.*, vol. 10, no. 1, pp. 69–83, 1979.
- [28] Y.-B. Zheng, T.-Z. Huang, T.-Y. Ji, X.-L. Zhao, T.-X. Jiang, and T.-H. Ma, "Low-rank tensor completion via smooth matrix factorization," *Appl. Math. Model.*, vol. 70, pp. 677–695, 2019.
- [29] J.-L. Wang, T.-Z. Huang, T.-H. Ma, X.-L. Zhao, and Y. Chen, "A sheared low-rank model for oblique stripe," *Appl. Math. Comput.*, vol. 360, pp. 167–180, 2019.
- [30] J.-H. Yang, X.-L. Zhao, T.-H. Ma, C. Yong, T.-Z. Huang, and M. Ding, "Remote sensing image destriping using unidirectional high-order total variation and nonconvex low-rank regularization," *J. Comput. Appl. Math.*, vol. 363, pp. 124–144, 2020.
- [31] J.-H. Yang, X.-L. Zhao, J.-J. Mei, S. Wang, T.-H. Ma, and T.-Z. Huang, "Total variation and high-order total variation adaptive model for restoring blurred images with cauchy noise," *Comput. Math. Appl.*, vol. 77, pp. 1255–1272, 2019.
- [32] T. Mach, L. Reichel, M. V. Barel, and R. Vandebril, "Adaptive cross approximation for ill-posed problems," *J. Comput. Appl. Math.*, vol. 303, pp. 206–217, 2016.
- [33] X. Zhou, F. Zhou, X. Bai, and B. Xue, "A boundary condition based deconvolution framework for image deblurring," *J. Comput. Appl. Math.*, vol. 261, no. 4, pp. 14–29, 2014.
- [34] C. Matonoha and Š. Papáček, "On the connection and equivalence of two methods for solving an ill-posed inverse problem based on FRAP data," *J. Comput. Appl. Math.*, vol. 290, pp. 598–608, 2015.
- [35] G. Zhou, H. Fang, C. Lu, S. Wang, Z. Zuo, and J. Hu, "Robust destriping of MODIS and hyperspectral data using a hybrid unidirectional total variation model," *Optik*, vol. 126, no. 7, pp. 838–845, 2015.
- [36] L. Zhuang and J. M. Bioucas-Dias, "Fast hyperspectral image denoising and inpainting based on low-rank and sparse representations," *IEEE J. Sel. Topics Appl. Earth Observ. Remote Sens.*, vol. 11, no. 3, pp. 730–742, Mar. 2018.
- [37] L. Zhuang and J. M. Bioucas-Dias, "Hyperspectral image denoising based on global and non-local low-rank factorizations," in *Proc. IEEE Int. Conf. Image Process.*, 2017, pp. 1900–1904.
- [38] Y. Chang, L. Yan, T. Wu, and S. Zhong, "Remote sensing image stripe noise removal: From image decomposition perspective," *IEEE Trans. Geosci. Remote Sens.*, vol. 54, no. 12, pp. 7018–7031, Dec. 2016.
- [39] Y.-T. Wang, X.-L. Zhao, T.-X. Jiang, L.-J. Deng, and Y.-T. Zhang, "A TV and group sparsity based tensor model for video rain streaks removal," *Signal. Image Process.*, vol. 73, pp. 96–108, 2019.
- [40] T.-X. Jiang, T.-Z. Huang, X.-L. Zhao, T.-Y. Ji, and L.-J. Deng, "Matrix factorization for low-rank tensor completion using framelet prior," *Inf. Sci.*, vol. 436, pp. 403–417, 2018.
- [41] W. He, H. Zhang, L. Zhang, and H. Shen, "Total-variation-regularized low-rank matrix factorization for hyperspectral image restoration," *IEEE Trans. Geosci. Remote Sens.*, vol. 54, no. 1, pp. 178–188, Jan. 2016.
- [42] Y. Chen, T.-Z. Huang, X.-L. Zhao, and L.-J. Deng, "Hyperspectral image restoration using framelet-regularized low-rank nonnegative matrix factorization," *Appl. Math. Model.*, vol. 63, pp. 128–147, 2018.
- [43] Y. Chang, L. Yan, H. Fang, and C. Luo, "Anisotropic spectral-spatial total variation model for multispectral remote sensing image destriping," *IEEE Trans. Image Process.*, vol. 24, no. 6, pp. 1852–1866, Jun. 2015.
- [44] W. Cao, Y. Chang, G. Han, and J. Li, "Destriping remote sensing image via low-rank approximation and nonlocal total variation," *IEEE Geosci. Remote Sens. Lett.*, vol. 15, no. 6, pp. 848–852, Jun. 2018.
- [45] Y. Chen, T.-Z. Huang, and X.-L. Zhao, "Destriping of multispectral remote sensing image using low-rank tensor decomposition," *IEEE J. Sel. Topics Appl. Earth Observ. Remote Sens.*, vol. 11, no. 12, pp. 4950–4967, Dec. 2018.
- [46] W. He, H. Zhang, H. Shen, and L. Zhang, "Hyperspectral image denoising using local low-rank matrix recovery and global spatial-spectral total variation," *IEEE J. Sel. Topics Appl. Earth Observ. Remote Sens.*, vol. 11, no. 3, pp. 713–729, Mar. 2018.
- [47] T.-X. Jiang, T.-Z. Huang, X.-L. Zhao, L.-J. Deng, and Y. Wang, "Fastderain: A novel video rain streak removal method using directional gradient priors," *IEEE Trans. Image Process.*, vol. 28, pp. 2089–2102, Apr. 2019.
- [48] X.-L. Zhao, W. Wang, T.-Y. Zeng, T.-Z. Huang, and M. K. Ng, "Total variation structured total least squares method for image restoration," *SIAM J. Sci. Comput.*, vol. 35, no. 6, pp. 1304–1320, 2013.
- [49] Y. Wang, J.-J. Peng, Y. Leung, D.-Y. Meng, and X.-L. Zhao, "Hyperspectral image restoration via total variation regularized low-rank tensor decomposition," *IEEE J. Sel. Topics Appl. Earth Observ. Remote Sens.*, vol. 11, no. 4, pp. 1227–1243, Apr. 2018.
- [50] E. J. Candès, M. B. Wakin, and S. P. Boyd, "Enhancing sparsity by reweighted l_1 minimization," *J. Fourier Anal. Appl.*, vol. 14, no. 5–6, pp. 877–905, 2008.
- [51] D. Giacobello, M. G. Christensen, M. N. Murthi, S. H. Jensen, and M. Moonen, "Enhancing sparsity in linear prediction of speech by iteratively reweighted l_1 -norm minimization," in *Proc. IEEE Int. Conf. Acoust., Speech, Signal Process.*, 2010, pp. 4650–4653.
- [52] W. He, H. Zhang, and L. Zhang, "Weighted sparse graph based dimensionality reduction for hyperspectral images," *IEEE Trans. Geosci. Remote Sens.*, vol. 13, no. 5, pp. 686–690, May 2016.

- [53] S. P. Boyd, N. Parikh, E. Chu, B. Peleato, and J. Eckstein, "Distributed optimization and statistical learning via the alternating direction method of multipliers," *Found. Trends Mach. Learn.*, vol. 3, no. 1, pp. 1–122, 2011.
- [54] J. Huang, T.-Z. Huang, L.-J. Deng, and X.-L. Zhao, "Joint-sparse-blocks and low-rank representation for hyperspectral unmixing," *IEEE Trans. Geosci. Remote Sens.*, vol. 57, no. 4, pp. 2419–2438, Apr. 2019.
- [55] D. L. Donoho, "De-noising by soft-thresholding," *IEEE Trans. Inform. Theory*, vol. 41, no. 3, pp. 613–627, May 1995.
- [56] J. Huang and T.-Z. Huang, "A nonstationary accelerating alternating direction method for frame-based Poissonian image deblurring," *J. Comput. Appl. Math.*, vol. 352, pp. 181–193, 2019.
- [57] X.-L. Zhao, F. Wang, and M. K. Ng, "A new convex optimization model for multiplicative noise and blur removal," *SIAM J. Imag. Sci.*, vol. 7, no. 1, pp. 456–475, 2014.
- [58] Y. Chen, T.-Z. Huang, L.-J. Deng, X.-L. Zhao, and M. Wang, "Group sparsity based regularization model for remote sensing image stripe noise removal," *Neurocomputing*, vol. 267, no. 6, pp. 95–106, 2017.
- [59] W. Zuo and Z. Lin, "A generalized accelerated proximal gradient approach for total-variation-based image restoration," *IEEE Trans. Image Process.*, vol. 20, no. 10, pp. 2748–2759, Oct. 2011.
- [60] R. W. Liu, L. Shi, W. Huang, J. Xu, S. C. H. Yu, and D. Wang, "Generalized total variation-based MRI Rician denoising model with spatially adaptive regularization parameters," *Magn. Reson. Imag.*, vol. 32, no. 6, pp. 702–720, 2014.
- [61] R. H. Yuhas, A. F. H. Goetz, and J. W. Boardman, "Discrimination among semi-arid landscape end members using the spectral angle mapper (SAM) algorithm," in *Proc. Summaries 4th JPL Airborne Earth Sci. Workshop*, 1992, pp. 147–149.
- [62] H. Shen and L. Zhang, "A MAP-based algorithm for destriping and inpainting of remotely sensed images," *IEEE Trans. Geosci. Remote Sens.*, vol. 47, no. 5, pp. 1492–1502, May 2009.



Jian-Li Wang received the B.S. degree in mathematics and applied mathematics from Neijiang Normal University, Neijiang, China, in 2017. She is currently working toward the Ph.D. degree with the School of Mathematical Sciences, University of Electronic Science and Technology of China, Chengdu, China.

Her current research interests include sparse and low-rank modeling for image processing problems.



Ting-Zhu Huang received the B.S., M.S., and Ph.D. degrees in computational mathematics from the Department of Mathematics, Xi'an Jiaotong University, Xi'an, China, in 1986, 1992, and 2001, respectively.

He is currently a Professor with the School of Mathematical Sciences, University of Electronic Science and Technology of China, Chengdu, China. His current research interests include scientific computation and applications, numerical algorithms for image processing, numerical linear algebra, preconditioning technologies, and matrix analysis with applications.

Dr. Huang is an Editor of the *Scientific World Journal*, *Advances in Numerical Analysis*, *Journal of Applied Mathematics*, *Journal of Pure and Applied Mathematics: Advances in Applied Mathematics*, and *Journal of Electronic Science and Technology*.



Xi-Le Zhao received the M.S. and Ph.D. degrees from the University of Electronic Science and Technology of China (UESTC), Chengdu, China, in 2009 and 2012, respectively.

He is currently a Professor with the School of Mathematical Sciences, UESTC. His current research interests include image processing, computer vision, and machine learning.



Jie Huang received the Ph.D. degree from the University of Electronic Science and Technology of China (UESTC), Chengdu, China, in 2013.

She is currently an Associate Professor with the School of Mathematical Sciences, UESTC. Her research interests include remote sensing and image processing.



Tian-Hui Ma received the B.S. and Ph.D. degrees in applied mathematics from the University of Electronic Science and Technology of China, Chengdu, China, in 2011 and 2017, respectively.

During 2016, he was a Visiting Student with the University of Texas at Dallas, Dallas, TX, USA. He is currently a Postdoctoral Researcher with the School of Mathematics and Statistics, Xi'an Jiaotong University, Xi'an, China. His current research interests include inverse problems in image processing and sparse optimization.



Yu-Bang Zheng received the B.S. degree in information and computing science from the Anhui University of Finance and Economics, Bengbu, China, in 2017. He is currently working toward the Ph.D. degree with the School of Mathematical Sciences, University of Electronic Science and Technology of China, Chengdu, China.

His current research interests include sparse and low-rank modeling for image processing problems.